UC Berkeley
UC Berkeley Previously Published Works

Title

A Technique to Quantify Very Low Activities in Regions of Interest With a Collimatorless Detector

Permalink

https://escholarship.org/uc/item/9rr3v9kv

Journal

IEEE Transactions on Medical Imaging, 43(8)

ISSN

Authors

Caravaca, Javier

Bobba, Kondapa Naidu

Du, Shixian

et al.

Publication Date

2024-08-01

DOI

Peer reviewed

A technique to quantify very low activities in regions of interest with a collimatorless detector

J. Caravaca [Member, IEEE],
University of California San Francisco, USA

K. N. Bobba,
University of California San Francisco, USA

S. Du,
University of California San Francisco, USA

R. Peter,
University of California Berkeley; University of California San Francisco, USA

G. T. Gullberg [Life Fellow, IEEE],
Lawrence Berkeley National Laboratory; University of California San Francisco, USA

A. P. Bidkar,
University of California San Francisco, USA

R. R. Flavell,
University of California San Francisco, USA

Y. Seo [Senior Member, IEEE]
University of California San Francisco, USA

Abstract

We present a new method to measure sub-microcurie activities of photon-emitting radionuclides in organs and lesions of small animals in vivo. Our technique, named the collimator-less likelihood fit, combines a very high sensitivity collimatorless detector with a Monte Carlo-based likelihood fit in order to estimate the activities in previously segmented regions of interest along with their uncertainties. This is done directly from the photon projections in our collimatorless detector and from the region of interest segmentation provided by an x-ray computed tomography scan. We have extensively validated our approach with ^{225}Ac experimentally in spherical phantoms and mouse phantoms, and also numerically with simulations of a realistic mouse anatomy. Our method yields statistically unbiased results with uncertainties smaller than 20% for activities as low as ~111 Bq (3 nCi) and for exposures under 30 minutes. We demonstrate that our method yields more robust recovery coefficients when compared to SPECT imaging with a commercial pre-clinical scanner, specially at very low activities. Thus, our technique is complementary to traditional SPECT/CT imaging since it provides a more accurate and precise organ and tumor dosimetry, with a more limited spatial information. Finally, our technique is specially significant in extremely low-activity scenarios when SPECT/CT imaging is simply not viable.

javier.caravacarodriguez@ucsf.edu .

Keywords

Gamma-ray imaging; Actinium-225 imaging; collimatorless gamma camera; region-of-interest likelihood fit

I.   Introduction

Targeted radionuclide therapy promises to enhance efficacy and decrease toxicity with respect to other cancer treatments techniques, leading to more effective patient treatment and care [1]. Targeted alpha therapy (TAT) has shown a superior response to treatment than beta therapy in several clinical trials, due to the much higher linear energy transfer of alpha particles over beta particles [2, 3]. A popular TAT isotope that has shown excellent performance in clinical trials is ^{225}Ac [4-6], whose decay chain (Fig. 1a) provides four alphas and two betas, used for therapeutic purposes, and several gamma- and x-ray emissions, which facilitate isotope imaging and potential alpha theranostics [1]. A key element to the development of novel TAT radiopharmaceuticals is determining their specificity, which is realized by the assessment of their biodistribution (BioD) in animal models of human tumors. A fundamental problem faced by TAT radiopharmaceutical development, and in particular ^{225}Ac, is that due to the higher efficacy and toxicity of alpha radiopharmaceuticals, the activities injected in small animals are more than two orders of magnitude smaller than those for beta-emitting drugs [7] or for standard radionuclide imaging. This defines a particular challenge for pre-clinical imaging of TAT radiopharmaceutical like ^{225}Ac, since imaging systems used for in-vivo dosimetry are not sensitive enough in the sub-microcurie range.

Single-photon emission computed tomography combined with x-ray computed tomography (SPECT/CT) could, in theory, provide quantitative in-vivo biodistributions of the ^{225}Ac progeny by forming three-dimensional images of the uptake of each isotope (Fig. 1b), as it has been demonstrated in phantoms with a commercial SPECT/CT system [8]. However, this required activities that are a 10- to 100-fold increase of those used in real TAT radiopharmaceutical studies in mice, and 1- to 24-hour exposures, which prohibits in-vivo imaging. A more recent study achieved ^{225}Ac in-vivo imaging of separated biodistributions of ^{221}Fr and ^{213}Bi from an ^{225}Ac injection in rabbits using a clinical SPECT/CT system [9], but again, the injected activity are a factor of 10 larger than the activities required for mice studies. Alternative in-vivo techniques have been proposed to assess radiopharmaceuticals BioD. Imaging of the Cherenkov light emitted by primary and secondary electron emissions in animals injected with ^{225}Ac has been demonstrated [10, 11]. However, this technique is only enabled at very high activities (~2 MBq or ~50 μCi), preventing longitudinal studies since the mice have to be euthanized shortly after the injection. Additionally, it can hardly differentiate between isotopes of the ^{225}Ac progeny, presenting a challenge for quantitative dosimetry. Several studies have shown larger hepatic and renal toxicity due to the separation of ^{225}Ac daughters from the original radiopharmaceutical [12], so pre-clinical BioD studies must have the ability to disentangle between the different contributions of each isotope in the decay chain. In sum, state-of-the-art radiation detection systems struggle to achieve the demanding sensitivities required to obtain a good signal-to-noise ratio for quantitative in

vivo analyses of sub-microcurie activities. Thus, to the extent of our knowledge, in vivo studies of the BioD of ^{225}Ac radiopharmaceuticals at the sub-microcurie level for each individual imageable isotope has not been achieved.

Due to the difficulties faced by in-vivo imaging and dosimetry, the study of BioD of ^{225}Ac radiopharmaceuticals is typically done ex vivo (Fig. 1c) by measuring the activity in tissue biopsies using gamma-ray counters [10] or imaging 2-D slices with autoradiography [13]. Important limitations of these methods are their inability to perform longitudinal studies in the same animal, which is critical to implement a dose fractionation plan based on dosimetry measurements (alpha theranostics [1]). Additionally, ex-vivo studies require several animals for each relevant time point in order to have a statically significant analysis of the biodistributions over time, resulting in a long and complex process and a large amount of animals being euthanized, with the subsequent ethical connotations.

In this manuscript we propose a new method to measure very low uptake levels in organs and tumors in vivo, enabling longitudinal BioD studies in the sub-microcurie range. Although our technique can be applied to virtually any photon emitting isotope, we focus our study on ^{225}Ac, given the high relevance of enabling low activity dosimetry of this radionuclide for TAT.

In order to dramatically increase the sensitivity by two or three orders of magnitude, we employ a collimatorless (CL) detector located almost in direct contact with the object [14, 15]. However, removing the collimator leads to a poor spatial resolution which makes conventional image reconstruction very difficult. Instead, we have developed a collimatorless likelihood fit (CL-LF) that can measure the activity in previously segmented regions of interests (ROI), such as organs or tumors, directly from the photon projections in the CL detector (Fig. 1d), thus circumventing the conventional voxel-level image reconstruction step. In particular, our method can provide activity measurements with only one projection, rather than relying on tomographic data. Similar techniques have been proposed in the literature for SPECT/CT using expectation maximization (EM [16]) algorithms [17, 18], but they have never been applied in combination with a CL detector.

We validated CL-LF with a Cadmium Zinc Telluride (CZT) system (Fig. 1e) in three different scenarios with ^{225}Ac: two experiments using our single-head CL prototype, and one with a simulated dual-head CL system upgrade. The first experiment uses spherical phantoms to provide a proof of principle of CL-LF and to characterize its performance in a simpler case. The second one validates CL-LF in a more complex scenario with a mouse phantom and realistic in-vivo conditions of size, ^{225}Ac radioactive dose, and time exposure. Finally, the third experiment studies the performance and limitations of CL-LF in a simulation of a dual-head detector configuration with a realistic digital mouse anatomy. In all experiments, we applied CL-LF to compute $\vec{A}$ and $\vec{\sigma}_A$ and compare them to the ground truth, accessible due to the usage of phantoms and simulation. CL-LF is applied separately to three different energy regions: the x-rays and low-energy gamma-rays between 70keV and 110 keV, the gamma-ray emission of ^{221}Fr (218 keV), and the one from ^{213}Bi (440 keV). Thus, we experimentally and theoretically validate CL-LF and characterize its accuracy, precision, and limitations, for each relevant ^{225}Ac photon emission. Finally, we study the

impact of uncertainties in CL-LF and we compare the performance of CL-LF against a state-of-the-art and commercial SPECT/CT pre-clinical scanner.

II.   Methods

In standard dosimetry algorithms, the individual voxel activities in the imaging space are determined and the total activity in a certain ROI is given as the sum of the individual voxel activities within that particular ROI (Fig. 1b). Typical image reconstruction algorithms use tomographic data to calculate individual voxel activities. Due to the large number of image voxels, this problem is extremely ill-posed when the number of detected counts is low, as it is the case in standard SPECT/CT with ^{225}Ac. Additionally, calculating the voxel uncertainties is highly non-trivial. In our proposed method, we use anatomical information from CT for a double purpose: to obtain a model of the subject for photon attenuation correction, and to identify the ROIs before the likelihood maximization step, substantially reducing the parameter space from the number of voxels to the number of ROIs. This represents a much more tractable problem due to the smaller number of free parameters. If we assume uniform activity in a given ROI, the shape of the projection is determined by the shape and location of the ROI, which are fixed by the CT information, and the only free parameter is the ROI activity. We perform a numerical likelihood fit that provides the best estimate of the activities in each ROI, as well as their uncertainties. This is enabled by a CL detector model based on Monte Carlo (MC) simulations used to calculate projections produced by any ROI. One of the advantages of using MC modeling is that photon transport effects such as attenuation in the subject or down-scattering of high energy gamma-rays are naturally taken into account in the model.

A.   Collimatorless system

Our detector head is designed and manufactured by IDEAS (Integrated Detector Electronics AS, Oslo, Norway) and consists of five CZT modules manufactured by Redlen Technologies (Sean Heights, Saanichton BC, Canada) of 25.4 mm × 25.4 mm with a thickness of 5 mm and a pixel pitch of 1.6 mm, for a total area of 127.8 mm × 25.4 mm. Each CZT module is connected to a read-out system designed by IDEAS with two ASICs, each instrumenting half of the pixels (128 of the 256 total per module). CZT modules, ASICs and cooling system are embedded in an aluminum case of 175 mm × 50 mm × 55 mm that makes the sensitive detector light tight. The surface of the CZT is located 0.9 mm from a 1mm-thick lid, so the sensitive detector is 1.9 mm from the top outer surface of the lid. This structure is referred as the detector head, and it is shown in Fig. 1e. The head is partially surrounded by lead bricks to provide shielding from laboratory radiation. The detector head is connected to a controller, which provides the interface to communicate with the ASICs and to collect data. The controller is connected to a computer through Ethernet and accessed using a desktop computer and the vendor's software. The detector head is affixed to a breadboard with a webcam positioned approximately 15 cm over the detector's surface and facing down to facilitate taking pictures of the location and position of the subjects (Fig. 1e). The dynamic range of the CZT readout allows recording energies below ~400 keV. Events above this energy are recorded in the overflow bin.

B.   Maximum likelihood fit

Let the elements in $\vec{\lambda}$ be the activity in each voxel j of the imaging space, and let the elements in $\vec{N}$ be the number of counts measured in each detector pixel i. The goal of standard radionuclide image reconstruction algorithms is to infer what is the most likely activity distribution $\vec{\lambda}'$ that corresponds to the observed sinogram $\vec{N}$,

$$\vec{\lambda}' = \underset{\vec{\lambda}}{\mathrm{argmax}}\, p(\vec{\lambda} \mid \vec{N}),$$

(1)

where $p(\vec{\lambda} \mid \vec{N})$ is the probability that we have $\vec{\lambda}$ if we measure $\vec{N}$. Given the very large number of voxels typically defined in the field of view, finding the $\vec{\lambda}$ that fulfills Eqn. (1) is a highly non-trivial problem. Moreover, for scenarios with low number of counts, this problem is very ill-posed. Since the ultimate interest of in-vivo dosimetry experiments is to determine the activities $\vec{A}$ in each ROI r (organs or tumors in our case), we introduce a probability that depends on $\vec{A}$ instead of $\vec{\lambda}$. This drastically reduces the number of free parameters and the complexity of the problem. Then, we can rewrite Eqn. (1) as

$$\vec{A}' = \underset{\vec{A}}{\mathrm{argmax}}\, p(\vec{A} \mid \vec{N})$$

(2)

where $p(\vec{A} \mid \vec{N})$ is the probability of having $\vec{A}$ observing $\vec{N}$. Applying Bayes rule,

$$p(\vec{A} \mid \vec{N}) = \frac{p(\vec{N} \mid \vec{A})\,p(\vec{A})}{p(\vec{N})},$$

(3)

$$\ln p(\vec{A} \mid \vec{N}) = \ln p(\vec{N} \mid \vec{A}) + \ln p(\vec{A}) - \ln p(\vec{N}).$$

(4)

where taking the logarithm does not change the position of the maximum in Eqn. (2). Since $\vec{A}$ is not constrained a priori, $\ln p(\vec{A})$ is simply a constant term that can be dropped from Eqn. (4) since it does not change the results of Eqn. (2). Although the $\ln p(\vec{N})$ term is also constant for a defined dataset $\vec{N}$ and it does not change the location of the maximum, we leave it for convenience in order to obtain an expression equivalent to [19]. Hence, the logarithm of the likelihood $\mathscr{L}$ is

$$\ln \mathscr{L} \equiv \ln p(\vec{A} \mid \vec{N}) = \ln p(\vec{N} \mid \vec{A}) - \ln p(\vec{N}),$$

$$(5)$$

whose expression we now derive.

We assume that $\vec{N}$ follows the statistics of independent Poisson experiments with mean value equal to the expected number of counts E_i in each pixel i. We also include a Gaussian constraint, $\mathcal{G}$, in order to account on the systematic uncertainty on the global detection efficiency δ, which is measured in Sec. II-G.3. This constraint penalizes the likelihood when values of δ are outside the limits of the measured standard deviation σ_δ. The number of expected counts per pixel E_i is calculated using a MC model and given by Eqn. (14). Thus,

$$p(\vec{N} \mid \vec{A}) = \prod_i p(N_i \mid \vec{A}) \times \mathcal{G}(\delta, \sigma_\delta) =$$

$$(6)$$

$$= \prod_i \frac{E_i(\vec{A})^{N_i} e^{-E_i(\vec{A})}}{N_i!} \times \frac{1}{\sigma_\delta \sqrt{2\pi}} e^{-\frac{1}{2}\left(\frac{\delta-1}{\sigma_\delta}\right)^2}$$

$$(7)$$

so the logarithm becomes

$$\ln p(\vec{N} \mid \vec{A}) \propto \sum_i \left[N_i \ln E_i(\vec{A}) - E_i(\vec{A}) - \ln N_i! \right] - \frac{1}{2}\left(\frac{\delta-1}{\sigma_\delta}\right)^2$$

$$(8)$$

where the constant terms have been removed. In a similar fashion, assuming $p(\vec{N})$ follows Poisson statistics with mean equal to the measured number of counts,

$$p(\vec{N}) = \prod_i \frac{N_i^{N_i} e^{-N_i}}{N_i!},$$

$$(9)$$

$$\ln p(\vec{N}) = \sum_i N_i - N_i \ln(N_i) + \ln(N_i!)$$

$$(10)$$

Substituting Eqn. (8) and Eqn. (10) in Eqn. (4) yields

$$\ln \mathcal{L} = \sum_i \left[-E_i(\vec{A}) + N_i - N_i \times \ln\left(\frac{N_i}{E_i(\vec{A})}\right) \right] - \frac{1}{2}\left(\frac{\delta-1}{\sigma_\delta}\right)^2,$$

(11)

For independent Poisson experiments, the $-2\ln\mathscr{L}$ behaves like a χ^2 distribution with degrees of freedom equal to the number of experiments (or number of pixels in our case) [19]. Thus, in practice, to obtain $\overrightarrow{A}$, we minimize the expression

$$-2\ln\mathscr{L} = 2 \times \sum_i \left[E_i(\overrightarrow{A}) - N_i + N_i \times \ln\left(\frac{N_i}{E_i(\overrightarrow{A})}\right) \right] + \frac{(\delta - 1)^2}{\sigma_\delta^2}.$$

(12)

This expression depends on a number of parameters (the number of ROIs plus the parameter δ) much smaller than the number of voxels. Hence, we apply a minimization algorithm that directly computes Eqn. (12) at every iteration step and estimate the shape of the likelihood to infer the most probable location of the minimum. This expression is minimized using the package Minuit [20] included in ROOT [21]. The MIGRAD algorithm [20], a popular algorithm in high-energy physics, is used to estimate the minimum and obtain $\overrightarrow{A}$. The MINOS algorithm [20] is used to compute the covariance matrix, $\mathscr{C}$, at the estimated minimum. The uncertainty of each activity estimation, $\overrightarrow{\sigma}_A$, is given by

$$\overrightarrow{\sigma}_A = [diag(\mathscr{C})]^{-1/2}.$$

(13)

C. Phantom experiments

1) Spherical phantom: Four spherical plastic shells of diameters 6 mm, 7 mm, 8 mm, and 10 mm and a wall thickness of 1 mm are filled with a solution of ^{225}Ac in water at a constant activity concentration of 629 kBq/mL (17 µCi/mL). The activities in each sphere are measured in a HIDEX automatic gamma-ray counter and correspond to 21.7±0.2 kBq (587.8±5.4 nCi), 42.2±0.3 kBq (1140.8±7.8 nCi), 69.8±0.4 kBq (1885.6±11.8 nCi), and 136.6±0.8 kBq (3690.9±22.1 nCi), respectively, from the smaller to the largest diameter. The gamma-ray counter has been previously calibrated with known activities of ^{225}Ac , measured by the distributor of the isotope. The experiment is carried out immediately after filling the phantom. We collected data for only one second with the four spherical phantoms in direct contact with the surface of the detector head. We tested three different inter-sphere separations of 10 mm, 20 mm, and 30 mm.

2) Mouse phantom: A 3D-printed mouse phantom manufactured by BIOEMTECH (Athens, Greece) of dimensions 98.9 mm × 27.5 mm × 22.7 mm with hollowed cavities resembling different organs (brain, thyroid, lungs, heart, liver, kidneys, and bladder) and two tumors (rear tumor on the flank and front tumor in the upper body) is used (see inset in Fig. 1e). 3D-printing plastic has a density and composition very close to that of soft tissue, which is ideal to mimic a realistic scenario. For our mouse phantom experiment, we filled the brain, liver, and rear tumor volumes with initial activities 7.9±0.1 kBq (214.6±3.7 nCi), 9.8±0.2 kBq (264.8±4.1 nCi), and 9.8±0.2 kBq (264.8±4.1 nCi), respectively, as measured

by our gamma-ray counter (HIDEX). The first experiment was approximately 24 hours after filling and repeated approximately every 10 days for a total of 64 days. Photon projections were collected over 20 minutes with the mouse phantom deployed in direct contact with the top surface of the detector head.

3) Digital phantom of realistic mouse anatomy: As opposed to the other two experiments that used real experimental data, here we performed a simulation experiment to explore the limits of our technique in a more complex case and with a dual-head detector. A CT scan of a live mouse [22] is segmented and imported into our simulations to model a realistic mouse anatomy. This includes the main organs (bone, lungs, muscle, heart, kidneys, spleen, liver and intestine) and a tumor xenograft in the left flank of about 0.02 cc. We simulate realistic organ activities as measured in a recent ex-vivo experiment that administered a single dose of 18.5 kBq (500 nCi) ^{225}Ac-DOTA-YS5 to mice [12]. We took three representative sets of measured activities at 2-days post-injection (p.i.), 7-days p.i., and 17-days p.i. (Table I). Body uptake (muscle) was negligible and not considered in our experiment. We produced one hundred simulated datasets for each set of activities to account for statistical fluctuations. We simulated a 30-minutes exposure for all cases.

D. Segmentation of the regions of interest

ROIs are determined by segmenting the CT images obtained from a commercial CT scanner [23]. We perform the segmentation using the ITK-SNAP open software [24] using the thresholding option. This determines the shape, orientation and position of each organ with respect to the detector. The segmented mouse phantom is a voxelized image of $185 \times 152 \times 659$ voxels of 0.16-mm side for a total dimension of 29.6 mm $\times$ 24.32 mm $\times$ 105.44 mm. The realistic digital mouse anatomy is segmented from CT images of a live mouse using a semi-manual method [22] and corresponds to a voxelized phantom of $108 \times 65 \times 200$ voxels of 0.35 mm side, for a total dimension of 37.8 mm $\times$ 22.75 mm $\times$ 70 mm. The segmentation of the spherical phantom is fully determined by the known diameters and positions of the spheres.

E. Detector simulation

The generation of ^{225}Ac gamma rays and x-rays, their propagation through the system geometry, and the interaction of primary and secondary particles with the detector material are modeled by the Geant4 simulation package [25]. ^{225}Ac decay is simulated using the standard Geant4 gun generator, which simulates gamma- and x-ray emissions with empirically determined branching ratios. The Livermore physics list is used to model the Compton scattering, photoelectric interaction, and electron multi-scattering. The detector head is modelled using the same dimensions as the original in Sec. II-A. Two different geometries are simulated: one with a single detector head for the spherical phantom (Fig. 4c) and the mouse phantom experiments (Fig. 5a), and another one with a dual detector head for the experiment with the digital mouse anatomy (Fig. 6a). In the dual-head configuration, each head is modelled after our validated single-head detector model.

The true deposited energy in each pixel is calculated as the sum of all the individual energy depositions in the pixel provided by Geant4 for each single event. An energy-dependent

Gaussian smearing is included to model the energy resolution characteristic of our CZT detector. This is measured as a function of the energy using different gamma-ray sources. An important effect known in CZT is the asymmetry in the energy spectrum due to the dependency of the charge induction efficiency (CIE) with the depth of interaction [26]. The CIE is simulated using a finite element method model and the charge transport equation is solved using the COMSOL MULTIPHYSICS software as described in [27]. The detected deposited energy is the result of multiplying the smeared true energy by the CIE factor.

F. Photon attenuation and phantom simulation

Photon attenuation in the subject is taken into account via our MC model. The voxelized model of the subject created from the segmented ROIs is input in our simulations, with different tissue materials assigned to each ROI. The datadriven physics models in Geant4 propagate photons through the subject geometry and materials. In this way we account for photon attenuation (absorption and scattering) in the subject. For Geant4 to accurately propagate photons, the ROI materials need to be defined based on their density and chemical composition. The assigned materials are as follows. The spherical phantom is simulated as spherical shells of the original diameter and thickness and of acrylic plastic material. The inner active material is simulated as water. The inactive body of the mouse phantom is simulated as acrylic plastic. The ROIs corresponding to empty cavities are simulated as air and those filled with the ^{225}Ac solution are simulated as water. For the digital mouse anatomy, we simulate each organ ROI with a different tissue material extracted from [28]. Since the soft tissue of the tumor is not found in [28], it is simulated as regular muscle.

G. CZT detector calibration

1) Relative pixel detection efficiency: The relative pixel detection efficiency ϵ_i is measured by deploying a radioactive source above the detector at a distance where the solid angle dependency is negligible. For this purpose, we use a 1 cm-diameter spherical source with ~0.1 MBq (~3 μCi) of ^{225}Ac located 50 cm from the detector head's front face. The number of counts with energy above 50 keV detected during a 2-hours exposure are calculated per pixel (Fig. 2a). We define ϵ_i as detection efficiency of pixel i with respect to the averaged pixel efficiency and it is calculated as the ratio of counts in i over the mean pixel efficiency (Fig. 2b). We only calibrate the relative efficiency since the calculation of the global detection efficiency is performed below.

2) Energy scale and resolution: We characterize the energy scale and resolution of our detector by deploying gamma-ray sources of known emission energies. The used gamma-ray emissions are 81 keV and 356 keV from ^{133}Ba, and 218 keV of ^{221}Fr (through ^{225}Ac decay). We also include a dataset with no source and a trigger threshold at zero to infer the position of the charge pedestal for zero-energy calibration. For each acquisition, we collect an energy spectrum and identify the position of the relevant peak as the center of the bin with most counts. The collection of channel numbers corresponding to each gamma-ray line including the zero-energy (pedestal) dataset, is interpolated in order to provide an energy-dependent energy calibration below 356 keV (Fig. 2c). Events above 356 keV are calibrated by a linear extrapolation of the last two points. The measured energy is very linear up to 218 keV. We compute the energy resolution as a function of energy using the same

point source data. Datasets are energy-calibrated as described previously and a Gaussian fit is performed in an energy window defined as $[E_p - 5\,\text{keV}, E_p + 15\,\text{keV}]$, where E_p is the energy at the peak. The energy window is asymmetric in order to avoid the Compton edge. The energy resolution is determined from the width of the Gaussian and reported as the full-width at half maximum (FWHM) in Fig. 2d.

3) Global detection efficiency: A global detection efficiency δ is defined for each energy window considered in the analysis (x-rays, ^{221}Fr, and ^{213}Bi). This is measured in situ by deploying spherical ^{225}Ac sources of different sizes and with different known activities at the center of the detector head's surface. A precise measurement of the activity in each sphere is given by a previously calibrated HIDEX gamma-ray counter. The total number of counts recorded in each experiment is compared to the expected number of counts predicted by our MC model. δ is defined as the ratio between the measured and the expected counts, which is shown in Fig. 2e as a function of the activity. Since δ is independent of the activity, we define it as a constant value equal to the average in each energy window, which correspond to $\delta_{x-ray} = 0.85 \pm 0.08$, $\delta_{Fr} = 0.67 \pm 0.11$, and $\delta_{Bi} = 0.36 \pm 0.06$. The quoted uncertainties include both the uncertainties in the data and in the MC added in quadrature. The difference between data and MC increases with energy, which is attributed to the detector becoming more inefficient at detecting high-energy depositions and to our CZT response model not being exact.

H. Forward-projection model

We applied CL-LF separately to the three most relevant photon emissions: x-rays, ^{221}Fr, and ^{213}Bi. The energy regions are 70keV to 110keV for x-rays, 205 keV to 230 keV for ^{221}Fr, and over 360 keV for ^{213}Bi. We calculate the number of expected counts for each energy region, $E_{r,i}$, for each detector pixel, i, and each ROI, r, by using our MC model. For each ROI, r, we assume a uniform distribution and simulate a total number of ^{225}Ac decays corresponding to an activity of $A_r^S = 18.5\,\text{kBq}$ (500nCi) and a time exposure of $T_r^S = 5\,\text{min}$. The superscript S indicates that these correspond to the activity and exposure simulated by our Monte Carlo framework. Thus, the number of counts detected in a given detector pixel i given the organ activities $\vec{A}$ and the exposure time T is given by

$$E_i(\vec{A}, \delta) = \delta \frac{1}{\varepsilon_i} T \sum_r A_r \frac{E_{r,i}}{A_r^S T_r^S} + B_i$$

(14)

where B_i is the number of background counts for a particular experiment in the pixel i. B_i is measured immediately after each dataset by acquiring data without ^{225}Ac source for the same time exposure T. ε_i is defined for each energy window. The ^{225}Ac is assumed to be in secular equilibrium to a good approximation, so the full decay chain is simulated for each event. By simulating the full ^{225}Ac decay chain and propagating the photons appropriately, we automatically account for the background component due to the down scattering of higher energy gamma-rays.

I. Systematic uncertainties study

This section is dedicated to assessing the stability of CL-LF in the presence of several uncertainties and unknowns. We intend to answer the question of how much the performance of CL-LF depends on these unknowns, namely, the potential heterogeneity of the activity distribution, the location and boundaries of the ROI activities, the photon attenuation, and the activity uptake in the body. We evaluate their impact by introducing variations in the digital mouse phantom model and quantifying the deviation from the nominal results. The evaluated systematic uncertainties are four. First, the miscoregistrations between the CT (segmentation) and the photon projections, which are studied in the form of translations and rotations. Second, the impact of photon attenuation using different attenuation scenarios. Third, the heterogeneity in the activity distribution, which is explored for two different heterogeneity models. And fourth, the presence of an activity background in the mouse body. A similar method is applied for all cases as follows.

The MC templates used for CL-LF are generated for the default phantom configuration. Then, forty MC datasets that include variations in the mouse phantom model are produced. These modified datasets are analyzed using the CL-LF with default MC templates, which are now different from the generated datasets due to the variations we deliberately introduced. These differences might result in deviations from the nominal results, which we evaluate quantitatively by computing the bias as

$$\text{Bias} \, [\%] = \frac{1}{n} \sum_{i=0}^{n} \frac{A_m^i - A_t^i}{A_t^i} \times 100$$

(15)

where A_m^i and A_t^i are the measured and true activities in ROI i, respectively, and the sum runs for all the ROIs, whose total number is n.

We use this method to evaluate the impact of translations in the segmentation parallel to the detector heads (horizontal plane), translations perpendicular to the detector heads (vertical axis), and rotations in an axis parallel to the detector heads (X axis). We also evaluate the impact of photon attenuation by comparing the default mouse model with a mouse phantom in which all the tissues are simulated as water. Additionally, we study the impact of the assumption of uniform activity within an ROI, we consider two extreme heterogeneity models: one in which hot clusters of 2.8 mm diameter are randomly interleaved with cold regions within the ROI, and another one in which the activity is just present in a 1.5 mm shell of the ROI, while the core of the ROI is cold (Fig. 7). Finally, this method is used to evaluate how the presence of an unaccounted activity background affects the CL-LF outcome. Two scenarios with activity concentrations of 86 Bq/g and 170 Bq/g in muscle are considered.

J. Comparison with multi-pinhole SPECT system

CL-LF is compared to a commercial multi-pinhole SPECT/CT pre-clinical scanner (VECTor4CT, MILabs, Houten, Netherlands [23]) to evaluate its capabilities with respect

to the state-of-the-art SPECT imaging (Fig. 1b). This scanner (shown in Fig. 3) is equipped with a tungsten collimator with 162 pinholes and three 9 mm-thick NaI detectors. We employ a 98-mm diameter high-energy, general-purpose collimator for rats and mice (HE-GP-RM) with a transversal and axial and field-of-view of 28 mm and 18 mm, respectively. This collimator is made of tungsten and features a sensitivity of 2% and a spatial resolution of 2.1mm for ^{99m}Tc.

For the image analysis, photopeak energy regions are centered on 82 keV for x-rays, 218 keV for ^{221}Fr and 440 keV for ^{213}Bi, with a 25% width. A width of 15% is selected for the background energy windows used in the triple-energy window correction implemented by the vendor. We calibrate the image quantification in the three energy windows (x-rays, ^{221}Fr, and ^{213}Bi) by following the vendor's suggested approach using a high activity vial to compute the calibration factor from number of counts to activity. After the system is calibrated, a mouse phantom equivalent to the one prepared in Sec. II-C.2 is imaged for 2 hours. The sensitivity of the collimator to detection of ^{225}Ac and its progeny is estimated by dividing the count rate in counts per second (cps) within each energy window by the total activity in the mouse phantom. Images of x-rays, ^{221}Fr , and ^{213}Bi are obtained by using the vendor's reconstruction algorithm [29] with 4 subsets and 25 iterations. Images for lower activities are emulated by randomly sampling a subset of the detected counts with a uniform probability. Finally, a CT-based attenuation correction is applied using the vendor's implementation.

We produce images equivalent to 133 kBq (3.6 μCi), 33 kBq (0.9 μCi), 11 kBq (0.3 μCi), 1.1 kBq (30 nCi), and 0.11 kBq (3 nCi) total activity for a 20-minutes exposure. We assess the quantitative imaging performance by computing the recovery coefficient (R) in spherical ROIs fully contained in the organ cavities as

$$R = \frac{A_m}{A_t}$$

(16)

where A_m and A_t are the measured and true activities, respectively. We compute R for our CL-LF and directly compare to the traditional SPECT method as a function of the total activity.

III.   Results

A.   Proof of principle with spherical phantoms

The energy spectrum collected during one minute of data is illustrated in Fig. 4a compared to the one obtained with the MC simulation. The three different energy regions of interest are highlighted in different color bands. The data and MC comparison show an excellent agreement. Photon projections for x-rays are shown in Fig. 4b for the three different inter-sphere separations and overlaid to a picture of the phantom. Expected photon projections are obtained using our MC simulation, whose geometry is illustrated in Fig. 4c. The activity measured by CL-LF in each sphere along with its uncertainty are shown in (Fig. 4d) for each

inter-sphere separation and energy window. In general, we obtain a good agreement with the ground truth, provided by the measured activities in a gamma counter.

B. Organ-level dosimetry in a mouse phantom

The segmentation process is shown in Fig. 5a along with a render of the simulated geometry and the illustration of a simulated photon projection. Experimental photon projections are shown in Fig. 5b for the different emissions overlaid to a picture of the mouse phantom. The activities measured by CL-LF are shown in Fig. 5c as a function of the day of the experiment and compared to the true activities. The ^{225}Ac decay curve is clearly visible and the measured activities are compatible with the ground truth for all ROIs, time points, and energy windows.

C. Theoretical performance and limitations

The digital mouse model from a live mouse (Fig. 6a) is used in this experiment along with a hypothetical dual-head detector. We compute the activities in each ROI of the one hundred simulated datasets using CL-LF. The mean, standard deviation, maximum and minimum activities in each ROI are shown in Fig. 6b, compared to the ground truth (Table I). No significant statistical bias is observed. The averaged relative uncertainties are shown as a function of true activity in Fig. 6c, revealing that a precision better than 20% for activities of the level of 200 Bq. Relative uncertainties are compared in Fig. 6d for each organ and day p.i. Additionally, we compared the uncertainty estimated by CL-LF to the standard deviation of the distribution of the measured activities and no significant deviation was found, indicating that CL-LF provides a good estimate of the uncertainties.

D. Impact of unknowns and systematic uncertainties

1) Segmentation co-registration uncertainty: the deviation from the true activity values are calculated for datasets including translations and rotations in the ROI segmentation, namely, parallel translations, perpendicular translations, and rotations. Results are shown in Fig. 7a, b and c. Translations are considered between 0 mm and 1 mm, and rotations between 0° and 2°. A null translation or rotation corresponds to the default case in Fig. 6.

2) Photon attenuation: results for datasets in which all the ROIs and body are composed by water are shown in Fig. 7d compared to the default case with realistic tissue materials in Sec. II-C.3. It is important to stress that the model used in CL-LF is the default model with realistic tissue in both cases.

3) Non-homogeneous activity distributions: the bias from the true activity obtained using datasets that include the implemented heterogeneity models are shown in Fig. 7e compared to the default uniform case. Once again, the model used in CL-LF is the default uniform model, while the MC datasets generated in this section implement the heterogeneity models. A 3D representation of the different models are shown in Fig. 7f for the liver.

4) Background activity: the impact of the presence of an unaccounted background activity concentration is shown in Fig. 7g. Averaged bias for x-rays and ^{221}Fr are lower

than 15%, while it reaches 80% for ^{213}Bi in the least favorable case with 170 Bq/g. A concentration below 100 Bq/g is considered reasonable according to [12].

E. Comparison with multi-pinhole SPECT system

The ^{225}Ac spectra obtained with the commercial multi-pinhole SPECT/CT system is shown in along with the three imaging energy windows (Fig. 8a). Mouse phantom images obtained with the commercial pinhole SPECT/CT system are shown in Fig. 8b for two different activities equivalent to a 20-minutes exposure. The computed sensitivities are 347 cps/MBq for x-rays, 599 cps/MBq for ^{221}Fr, and 653 cps/MBq for ^{213}Bi. The recovery coefficient R as a function of the total activity are compared to those obtained with CL-LF in Fig. 8c. In general, pinhole SPECT shows much larger fluctuations, reflected in the larger uncertainties, and deviations from the unity than CL-LF, whose R is very robust in the explored range of activities.

IV. Discussion

We have presented and validated a technique that can measure nanocurie levels of ^{225}Ac in organs and tumors of small animals in minutes. Our studies demonstrate that CL-LF is statistically unbiased and that it provides accurate uncertainties. We used CT information to obtain a precise model of the subject and to take into account photon attenuation using MC simulation, as well as for ROI segmentation and subsequent quantification.

A similar technique using an EM-based method was demonstrated for traditional SPECT/CT with collimators in [18]. Our method takes a different approach by using CL detectors and also a likelihood fit that calculates uncertainties in each ROI activity.

We measured microcurie activities in hot spheres with a one-second exposure, which is equivalent to 222 Bq (6 nCi) with a 20-minutes exposure. Our method does not provide a planar or tomographic image, so we cannot talk of spatial resolution in the traditional way and we cannot directly compare to collimated systems, but we provide some evaluation in the following sentences. The minimum distance between two spheres that the raw projections could resolve when the spheres are in contact with the detector was 20 mm. However, we could measure the activity in spheres located as close as 10 mm with a precision ranging between 20% to 40%, depending on the size and location of the sphere with respect to the others. The spatial resolution of the ROIs is determined by the smallest size that can be identified using the anatomical image. This would be a combination between the spatial resolution of the anatomical image obtained from CT (300 μm in our case) or MRI, and the imaging contrast.

For the mouse phantom experiment, the relative uncertainties for the measurements in Fig. 5c are all below 20%, indicating that we can reach a precision of ~20% for ~100 Bq (~3 nCi) with a 20-minutes exposure for the three main ^{225}Ac emissions: x-rays, ^{221}Fr , and ^{213}Bi.The uncertainty in the activity of a particular ROI heavily depends on the size and shape of the ROI, but also on its activity and its position with respect to the other ROIs. We assume our experiments and simulations to be realistic and representative of real scenarios, but the uncertainty in each ROI will depend on each particular case.

We explored the limitations of this technique in realistic settings using a digital mouse anatomy with simulated activity uptakes from a real experiment [12]. This includes ^{225}Ac uptake in tumor as well as in healthy organs. Major organs representing the largest uptakes are considered: liver, kidneys, heart, lungs, spleen, and bone. The calculated relative uncertainties are below 20% for organs with activities of the order or above 200 Bq (5.4 nCi), as shown in Fig. 6c. This is similar to the previous mouse phantom experiment. Also, no significant bias is observed from Fig. 6b.

This experiment also served to explore the impact on the accuracy and precision of CL-LF of possible systematic uncertainties in the CT and segmentation co-registration. As shown in Fig. 7a and b, the averaged bias introduced by parallel translations of 1 mm is below 25%. CL-LF is more sensitive to perpendicular translations and relatively large deviations of 100% can be observed for perpendicular translations of 1 mm. However, sub-millimeter alignment and co-registration are feasible, so these effects, although important, could be controlled, as we demonstrated experimentally with a real single-head system with a spherical and a mouse phantom. In this study, we neglected the blood uptake since it is distributed throughout the full subject, and thus, the concentration is estimated to be below 100 Bq/g [12]. We quantified the effect of the presence of an activity concentration evenly distributed in the muscle to be very small for x-rays and ^{221}Fr , and to increase the average bias up to 50% for ^{213}Bi in our particular case study. This is likely due to the lower count rate for ^{213}Bi. This suggests that background effects can have a non-negligible effect in CL-LF. This could be mitigated by enlarging the statistics of the dataset by increasing the acquisition time.

Compared to the standard ex-vivo BioD methodology, CL-LF provides similar or better uncertainties. The most important impact of CL-LF is that it enables longitudinal BioD studies in the same individual, making possible to perform quantitative alpha theranostic studies in pre-clinical settings. In addition, our technique does not require mice dissection nor euthanasia of large population of mice. This is more straightforward implementation which saves a considerable amount of time and it also spares animal lives.

We demonstrated that the usage of CL detectors provides the required sensitivity for the dosimetry study of sub-microcurie levels of ^{225}Ac, which are the typical injected levels for TAT radiopharmaceutical BioD studies. For our single-head detector, we measured a sensitivity of 24150 cps/MBq for x-rays, 5733 cps/MBq for ^{221}Fr, and 2759 cps/MBq for ^{213}Bi. This represents an increase of a factor ~70 for x-rays, ~10 for ^{221}Fr, and ~4 for ^{213}Bi with respect to the pinhole SPECT system. This is with only one detector head and 5 mm-thick CZT detectors, to be compared to the much larger cylindrical coverage of the pinhole SPECT system and its thicker (9 mm) detectors. The sensitivities of our system doubled in the dual-head detector geometry. Other advantages of CL systems are the elimination of background due to scattering in the collimator and characteristic x-rays produced by the interaction of photons with the collimator.

Regarding measurement of organ activities, the recovery coefficient obtained for CL-LF are very close to 1 for the full range of activities under study up to 9 nCi, with very small fluctuations observed between the different ROIs. On the other hand, the pinhole SPECT

system successfully recovers the original true activity in each ROI only for activities above 300 nCi, with large fluctuations between ROIs due to the poor signal to noise ratio, as observed in Fig. 8c.

Despite the superior performance of CL-LF, we have envisioned this method not to substitute imaging, but to complement it in those cases where imaging does not provide a precise dosimetry due to the extremely low number of counts. Photon imaging is still desirable when possible since it does not rely on the subject's anatomy to define the shape of the biodistributions.

Our current implementation of CL-LF assumes uniform activities within each ROI. We have applied this default CL-LF to synthetic data that simulates activity heterogeneity and shown that the averaged bias introduced by these two models (clustered and shell) are below 25%, as shown by the averaged values in Fig. 7e. Also, the uncertainty introduced by a potential heterogeneity decreases the precision of CL-LF to 60%, as seen from the size of the error bars in Fig. 7e. We consider these models extreme cases of heterogeneity, since they present clear hot and cold regions, which is not often the case in realistic settings. CL-LF also allows to further segment organs in sub-organ ROIs in order to measure the activity in different regions of the same organ. Additionally, CL-LF could also implement realistic heterogeneity models in order to perform hypothesis testing and reduce uncertainty. We save exploration of those scenarios for future dedicated papers.

The choice of a gradient-based estimation of the likelihood maximum (Minuit [20]) is justified by the fact that this method provides a very fast estimation (seconds) of the location of the maximum along with its derivative, which provides both the estimated activities and their uncertainties, taking into account correlations between them. Alternative iterative methods, such as the popular EM [16], could also be implemented in a version of CL-LF. However, a direct comparison of our likelihood maximization method and EM have not been performed in this paper.

Our technique could still be further improved in the hardware and software planes, namely: a) prototype upgrade: we show that a dual-head detector could provide uncertainties better than 20 % for ROI activities as low as 111 Bq (3 nCi). In particular, our simulation predicts that the activity in the three main ROIs (tumor, liver and kidneys), can be determined even 17 days after the injection. b) Detector performance: we observe some noise in the projections obtained with higher energy photons (mainly in the ^{213}Bi energy window, Fig. 5b) that is attributed to a technical limitation of our detector, which is optimized for the energy range below 300 keV. Despite the noise, ^{213}Bi activities could still be measured with similar precision than the other emissions. c) Energy resolution: x-ray emissions where treated together due to the energy resolution of our detector not allowing a clear separation. A detector with better energy resolution, such as high-purity germanium, could potentially resolve some of the x-ray peaks. d) Detector model: the small discrepancy observed between 100 keV and 200 keV between data and MC (Fig. 4a) is attributed to the fact that our CZT detector model is not exact. In particular, charge sharing is not modeled. A better detector model could improve the results. e) CL-LF extension: since our ^{225}Ac sample is in secular equilibrium, we have not explored the impact of different distributions of ^{221}Fr and ^{213}Bi.

CL-LF could be easily extended to perform a joint likelihood fit of the three energy windows in order to separately measure different levels of each isotope, but we consider this to be out of the scope of the current paper. f) Usage of CT contrast or MRI: since our method relies heavily in a precise segmentation, a better anatomical imaging technique would benefit CL-LF. Contrast CT is used in [22] to segment the soft-tissue organs and tumors in live mice and to produce the realistic digital mouse phantom used in this paper, showing that this technique is feasible. The usage of MRI could further improve segmentation and mitigate potential uncertainties in CL-LF, but we have not explored that possibility on this paper.

V.   Conclusion

In summary, CL-LF can provide in-vivo BioD measurements of sub-microcurie levels of ^{225}Ac in mice phantoms mimicking mice imaging conditions with ^{225}Ac. This method is not exclusive to ^{225}Ac, but it can be easily extended to any photon emitting radionuclide, including other promising TAT isotopes like ^{227}Th [30]. We have shown that ^{225}Ac organ dosimetry with CL-LF outperforms that with traditional pinhole SPECT/CT for activities below 300 nCi. We have envisioned CL-LF as a complementary method that can be used to obtain more accurate organ dosimetry when imaging is limited due to the extremely low number of counts or simply not available. However, imaging is still desirable when possible, since it does not assume a prior shape of the biodistributions from the anatomy of the subject. Furthermore, this method has the potential for human translation. Given the challenge of ^{225}Ac imaging in the clinic [31, 32], our method could provide an alternative solution.

Acknowledgments

References

[1]. Sgouros G et al. "Radiopharmaceutical therapy in cancer: clinical advances and challenges". In: Nature reviews Drug discovery 19.9 (2020), pp. 589–608. [PubMed: 32728208]

[2]. Elgqvist J et al. "The potential and hurdles of targeted alpha therapy–clinical trials and beyond". In: Frontiers in oncology 3 (2014), p. 324. [PubMed: 24459634]

[3]. Tafreshi NK et al. "Development of targeted alpha particle therapy for solid tumors". In: Molecules 24.23 (2019), p. 4314. [PubMed: 31779154]

[4]. A Scheinberg D and R McDevitt M. "Actinium-225 in targeted alpha-particle therapeutic applications". In: Current radiopharmaceuticals 4.4 (2011), pp. 306–320. [PubMed: 22202153]

[5]. Morgenstern A et al. "An overview of targeted alpha therapy with 225Actinium and 213Bismuth". In: Current radiopharmaceuticals 11.3 (2018), pp. 200–208. [PubMed: 29732998]

[6]. Sathekge M et al. "225 Ac-PSMA-617 in chemotherapy-naive patients with advanced prostate cancer: a pilot study". In: European journal of nuclear medicine and molecular imaging 46 (2019), pp. 129–138. [PubMed: 30232539]

[7]. Moroz A et al. "Theranostic Targeting of CUB Domain Containing Protein 1 (CDCP1) in Pancreatic CancerTreating Cancer by Targeting CUB Domain Containing Protein 1". In: Clinical Cancer Research 26.14 (2020), pp. 3608–3615. [PubMed: 32341034]

[8]. Robertson AK et al. "Multi-isotope SPECT imaging of the 225Ac decay chain: feasibility studies". In: Physics in Medicine & Biology 62.11 (2017), p. 4406. [PubMed: 28362640]

[9]. Du Y et al. "Preliminary evaluation of alpha-emitting radioembolization in animal models of hepatocellular carcinoma". In: Plos one 17.1 (2022), e0261982. [PubMed: 35061763]

[10]. Pandya DN et al. "Preliminary therapy evaluation of 225Ac-DOTA-c (RGDyK) demonstrates that Cerenkov radiation derived from 225Ac daughter decay can be detected by optical imaging for in vivo tumor visualization". In: Theranostics 6.5 (2016), p. 698. [PubMed: 27022417]

[11]. Poty S et al. "Leveraging bioorthogonal click chemistry to improve 225Ac-radioimmunotherapy of pancreatic ductal adenocarcinoma". In: Clinical Cancer Research 25.2 (2019), pp. 868–880. [PubMed: 30352909]

[12]. Bidkar AP et al. "Treatment of prostate cancer with CD46 targeted 225Ac alpha particle radioimmunotherapy". In: Clinical Cancer Research 22.3291 (2023), pp. 2022–10.

[13]. Peter R et al. "Small-scale (sub-organ and cellular level) alpha-particle dosimetry methods using an iQID digital autoradiography imaging system". In: Scientific Reports 12.1 (2022), p. 17934. [PubMed: 36289434]

[14]. Caravaca J et al. "Compton and Proximity Imaging of Ac In Vivo With a CZT Gamma Camera: A Proof of Principle With Simulations". In: IEEE Transactions on Radiation and Plasma Medical Sciences 6.8 (2022), pp. 904–915. [PubMed: 36338821]

[15]. Walker KL et al. "Un-collimated single-photon imaging system for high-sensitivity small animal and plant imaging". In: Physics in Medicine & Biology 60.1 (2014), p. 403. [PubMed: 25504038]

[16]. Levitan E and Herman GT. "A maximum a posteriori probability expectation maximization algorithm for image reconstruction in emission tomography". In: IEEE transactions on medical imaging 6.3 (1987), pp. 185–192. [PubMed: 18244020]

[17]. Carson RE. "A maximum likelihood method for region-of-interest evaluation in emission tomography." In: Journal of computer assisted tomography 10.4 (1986), pp. 654–663. [PubMed: 3488338]

[18]. Li Z et al. "A Projection-Domain Low-Count Quantitative SPECT Method for alpha-Particle-Emitting Radiopharmaceutical Therapy". In: IEEE Transactions on Radiation and Plasma Medical Sciences 7.1 (2022), pp. 62–74. [PubMed: 37201111]

[19]. Baker S and Cousins RD. "Clarification of the use of chi-square and likelihood functions in fits to histograms". In: Nuclear Instruments and Methods in Physics Research 221.2 (1984), pp. 437–442.

[20]. James F and Roos M. "Minuit: A System for Function Minimization and Analysis of the Parameter Errors and Correlations". In: Comput. Phys. Commun 10 (1975), pp. 343–367.

[21]. Brun R and Rademakers F. "ROOT—An object oriented data analysis framework". In: Nuclear instruments and methods in physics research section A: accelerators, spectrometers, detectors and associated equipment 389.1-2 (1997), pp. 81–86.

[22]. Rosenhain S et al. "A preclinical micro-computed tomography database including 3D whole body organ segmentations". In: Scientific data 5.1 (2018), pp. 1–9. [PubMed: 30482902]

[23]. Goorden MC et al. "VECTor: a preclinical imaging system for simultaneous submillimeter SPECT and PET". In: Journal of Nuclear Medicine 54.2 (2013), pp. 306–312. [PubMed: 23077113]

[24]. Yushkevich PA et al. "User-Guided 3D Active Contour Segmentation of Anatomical Structures: Significantly Improved Efficiency and Reliability". In: Neuroimage 31.3 (2006), pp. 1116–1128. [PubMed: 16545965]

[25]. Agostinelli S et al. "GEANT4—a simulation toolkit". In: Nuclear instruments and methods in physics research section A: Accelerators, Spectrometers, Detectors and Associated Equipment 506.3 (2003), pp. 250–303.

[26]. Myronakis ME and Darambara DG. "Monte Carlo investigation of charge-transport effects on energy resolution and detection efficiency of pixelated CZT detectors for SPECT/PET applications". In: Medical physics 38.1 (2011), pp. 455–467. [PubMed: 21361214]

[27]. Huh Y et al. "Simulation studies of a full-ring, CZT SPECT system for whole-body imaging of 99mTc and 177Lu". In: Medical Physics (2023).

[28]. Valentin J. "Basic anatomical and physiological data for use in radiological protection: reference values: ICRP Publication 89: Approved by the Commission in September 2001". In: Annals of the ICRP 32.3-4 (2002), pp. 1–277.

[29]. Goorden MC et al. "Accelerated image reconstruction by a combined dual-matrix dual-voxel approach". In: Physics in Medicine & Biology 65.10 (2020), p. 105014. [PubMed: 32208374]

[30]. Frantellizzi V et al. "Targeted alpha therapy with thorium-227". In: Cancer biotherapy & radiopharmaceuticals 35.6 (2020), pp. 437–445. [PubMed: 31967907]

[31]. Gosewisch A et al. "Image-based dosimetry for 225 Ac-PSMA-I&T therapy using quantitative SPECT". In: European journal of nuclear medicine and molecular imaging 48 (2021), pp. 1260–1261. [PubMed: 32959113]

[32]. Delker A et al. "Biodistribution and dosimetry for combined [177Lu] Lu-PSMA-I&T/[225Ac] Ac-PSMA-I&T therapy using multi-isotope quantitative SPECT imaging". In: European Journal of Nuclear Medicine and Molecular Imaging (2023), pp. 1–11.
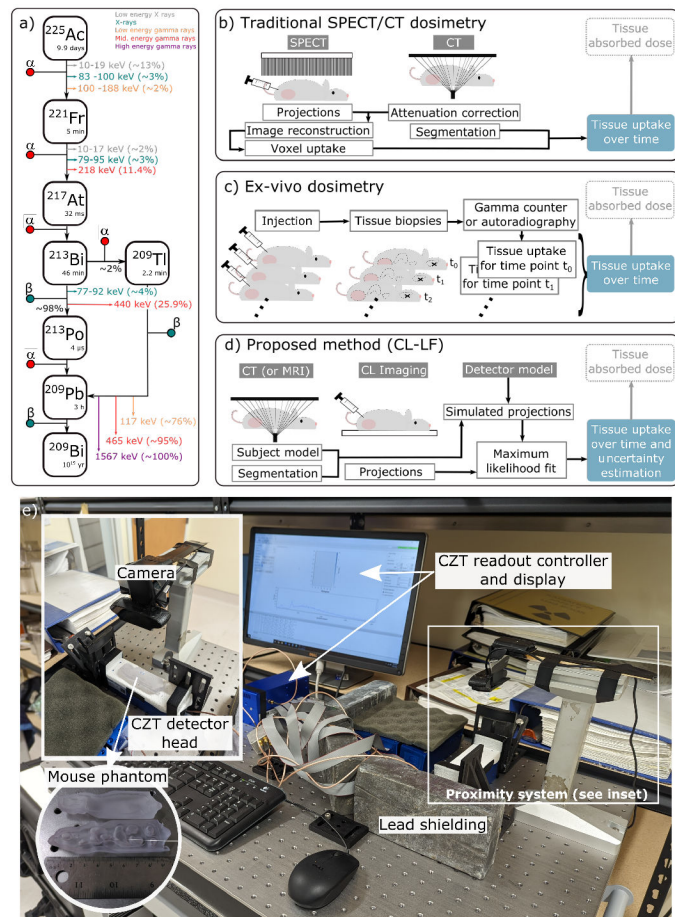
Fig. 1.
a) ^{225}Ac decay chain. Photon emissions with relatively low branching ratios are not reported. **b)** Traditional SPECT/CT dosimetry. **c)** Ex-vivo dosimetry methodology. **d)** Our proposed method. **e)** System configuration and close-up of the open mouse phantom.
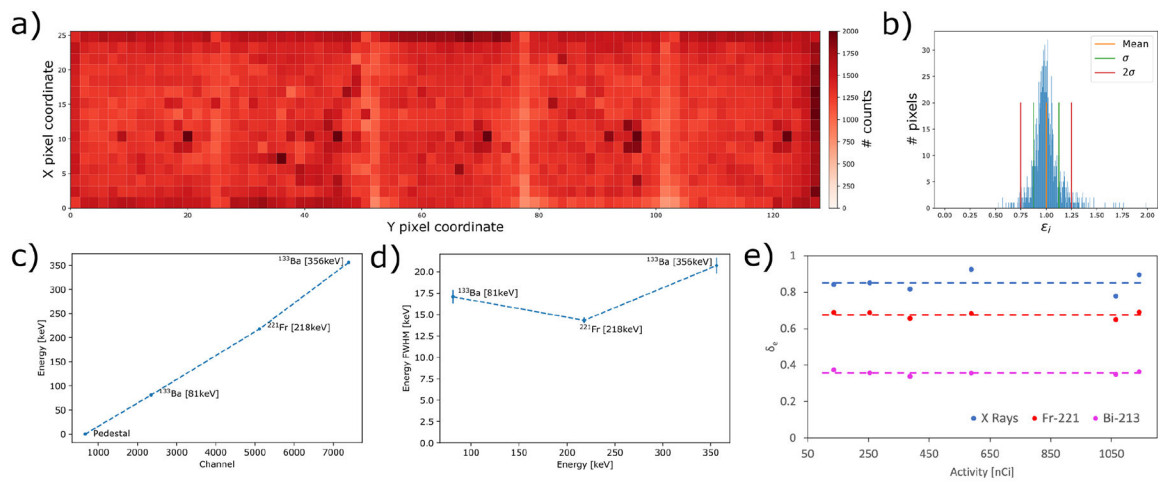
Fig. 2.

Summary of detector calibration. **a)** Number of counts in each pixel for a uniform dataset used to compute the relative pixel efficiency. **b)** Relative pixel efficiency distribution for all the pixels in the detector (ε_i). The 1σ and 2σ boundaries from the mean ε_i are shown in green and red, respectively. **(c)** True energy versus detector channel number. The uncertainties are invisible due to being very small. The dotted line corresponds to the interpolation used as energy calibration. **(d)** Energy resolution as a function of energy as measured in our detector and the interpolation (dotted line) used in the MC simulations. **e)** Global detection efficiency as a function of ^{225}Ac activity for each energy window. The dotted lines correspond to the averaged value used as δ.

Fig. 3.
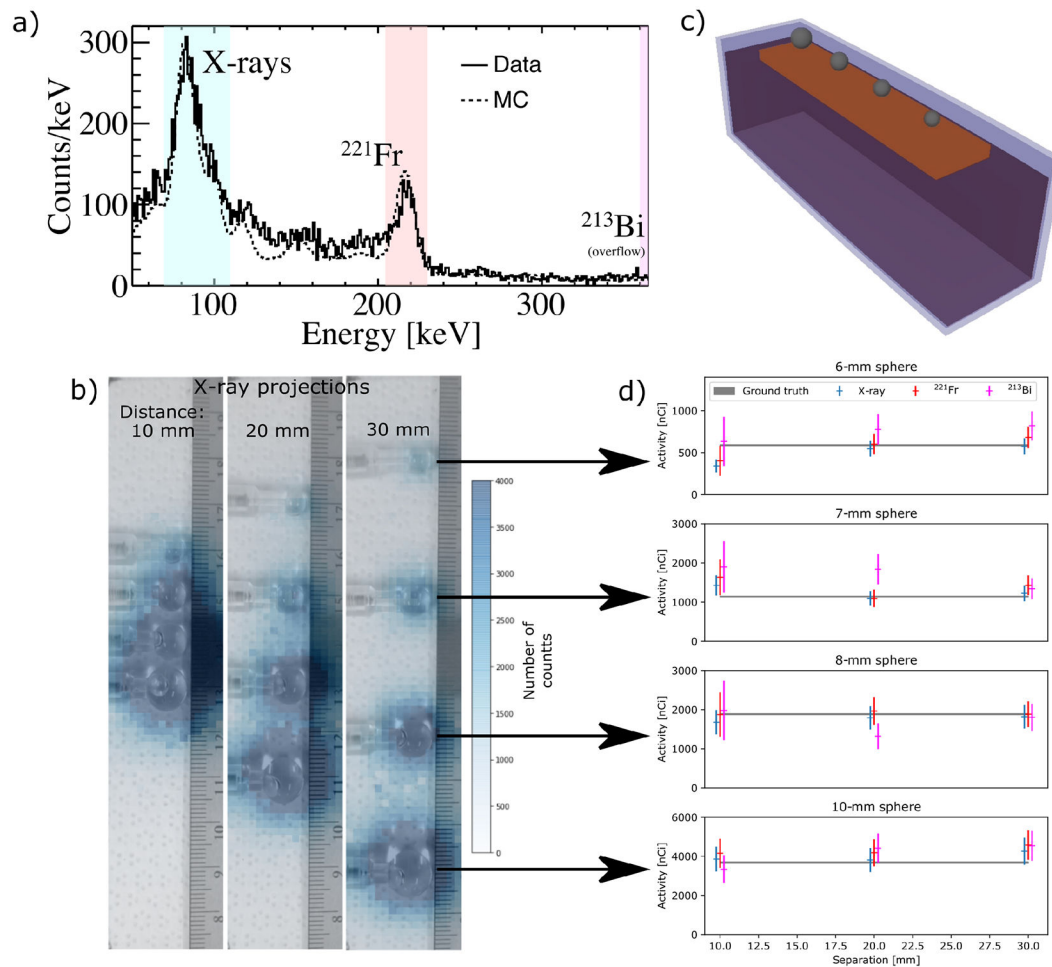Our commercial preclinical SPECT/CT scanner [23] used to compare to CL-LF.

Fig. 4.
Results of the spherical phantom experiments. **a)** Energy spectrum of approximately 0.27 MBq (7.3 μCi) of ^{225}Ac after an exposure of one second taken with our CL detector and compared to the simulation. The three energy windows used in the analysis are highlighted in cyan (x-rays), red (^{221}Fr), and magenta (^{213}Bi). **b)** Pictures of the different spherical phantom configurations overlaid with x-ray projections. **c)** Render of the simulated spherical phantoms in the 30-mm separation configuration. **d)** Activities and uncertainties estimated by CL-LF (markers) for each sphere and distance, compared to the true activities (gray bands).
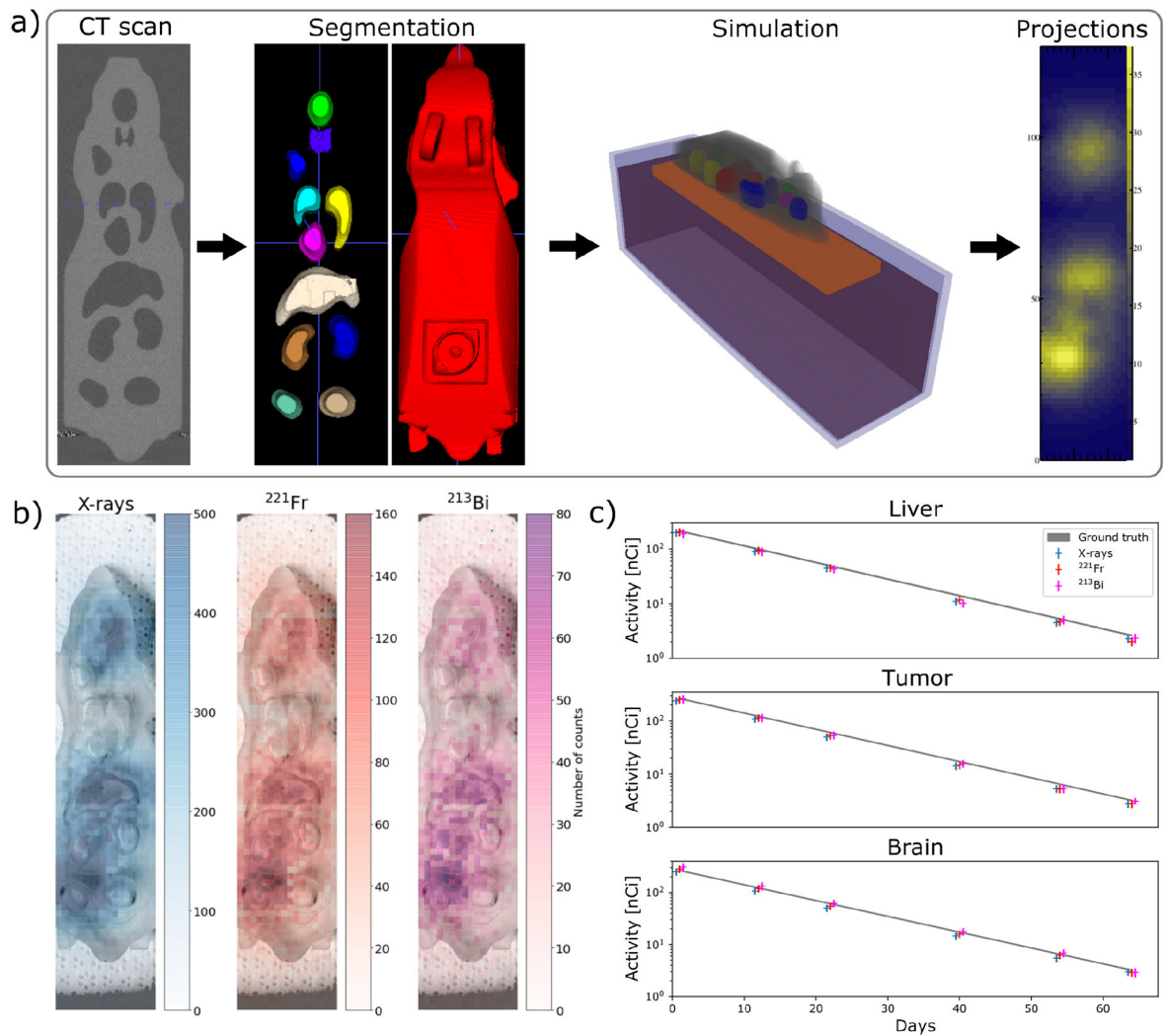
Fig. 5.
Results of the mouse phantom experiments. **a)** Illustration of the method used to obtain the simulated organ projections used in CL-LF. **b)** Overlay of mouse phantom pictures with projections for the three energy windows for 20-minutes exposure in day 1 after filling with ^{225}Ac. **c)** Measured activities and uncertainties (markers) as a function of the day the phantom was filled, compared to the true activity (gray bands).
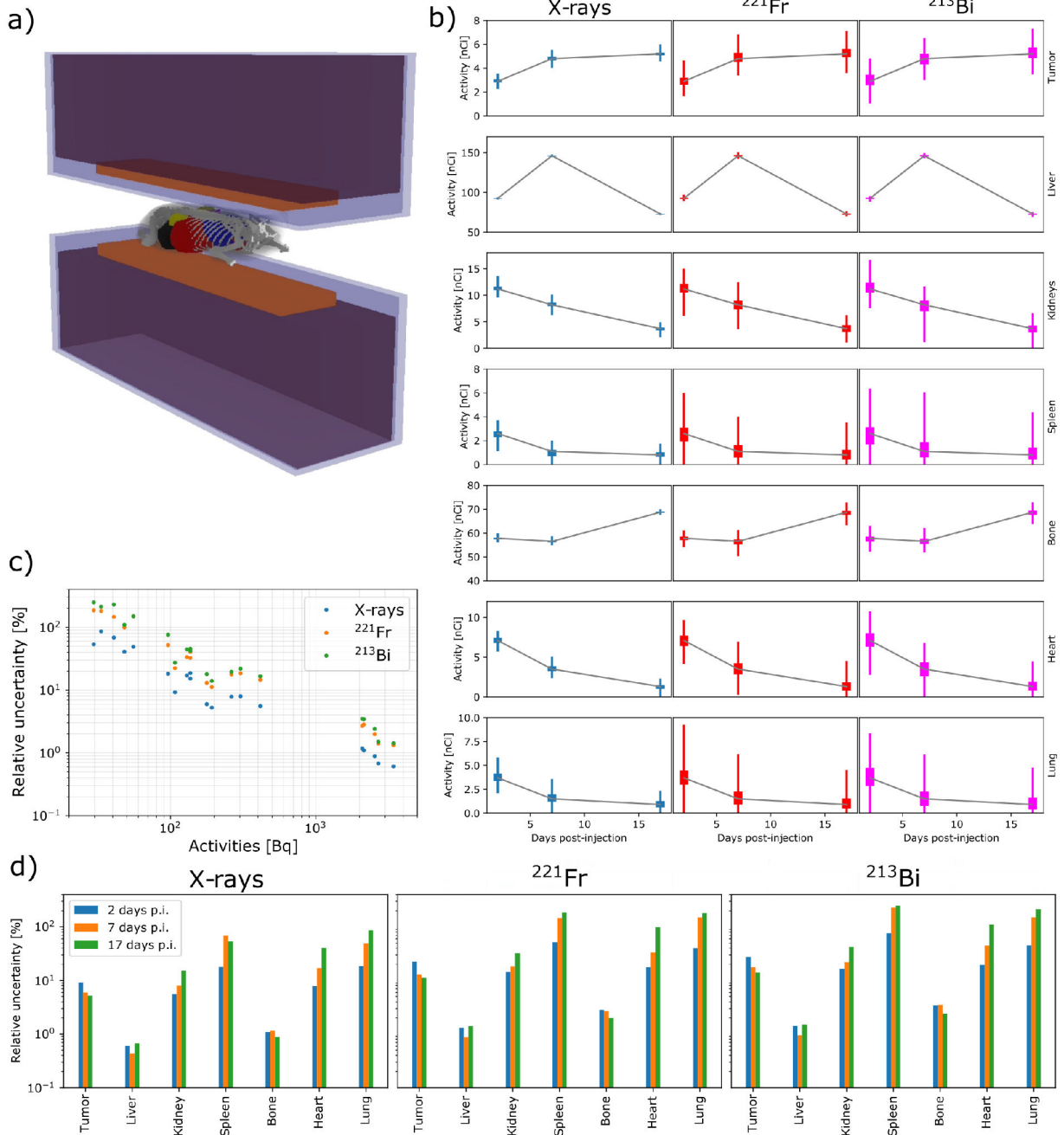
Fig. 6.
Results of the simulation experiment with a dual-head CL detector and a realistic mouse anatomy. **a)** Render of the simulated dual-head CL system with the realistic mouse anatomy. **b)** Measured activities (color) compared to the true activities (gray bands) for each emission and organ or tumor as a function of the day p.i. The boxes correspond to the standard deviation of the measured activities and the lines to the maximum and minimum measured values. **c)** Relative uncertainties as a function of true activities for the three relevant emissions. **d)** Averaged uncertainty as estimated by CL-LF for each organ, emission, and day p.i.
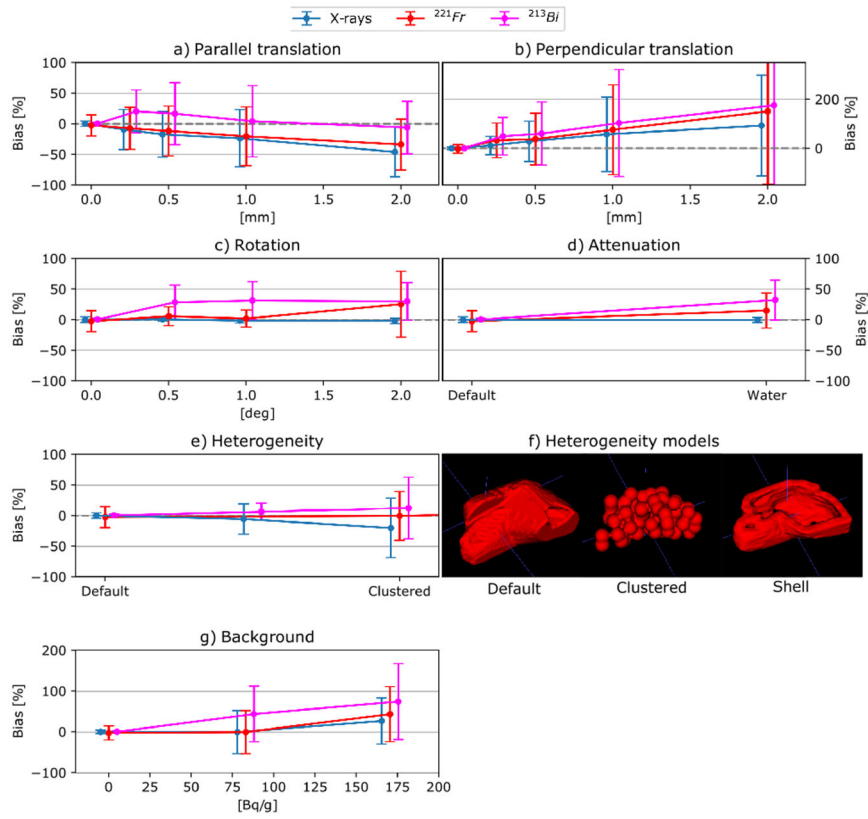
Fig. 7.
Evaluation of the impact of potential uncertainties in CL-LF: **a)** translation of an axis parallel to the detector heads, **b)** translation of the axis perpendicular to the detector heads, **c)** rotation in an axis parallel to the detector heads, **d)** photon attenuation for different tissue compositions, **e)** heterogeneity on the ^{225}Ac uptake with illustration of the models for the liver in **f)** (a section of the shell model is shown to highlight that the inner region is a cold region), and **g)** presence of background.
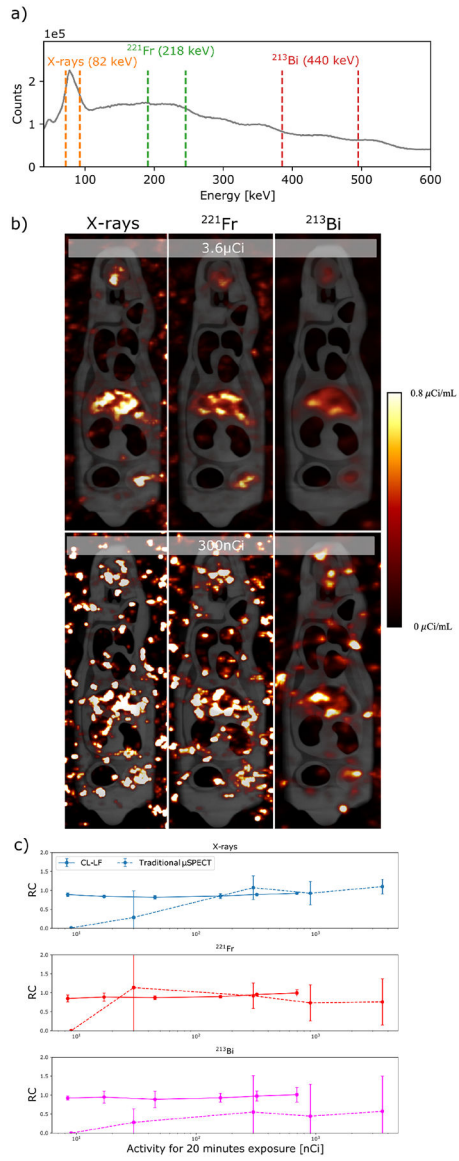
Fig. 8.
(a) ^{225}Ac energy spectrum obtained with the commercial SPECT/CT system (VECTor4CT [23]). **(b)** Images of a mouse phantom filled with ^{225}Ac in the commercial SPECT/CT. **(c)** Recovery coefficients as a function of the activity equivalent to a 20-minutes exposure. Values and uncertainties on the first point of the traditional SPECT recovery coefficient could not be precisely calculated and are set to zero.

TABLE I

SIMULATED TISSUE ACTIVITIES BASED ON MEASURED BIODISTRIBUTIONS OF ^{225}Ac-DOTA-YS5 [12].

Simulated activities [nCi]	Day 2	Day 7	Day 17
Tumor	2.9	4.8	5.2
Liver	92.5	146.0	72.8
Kidney	11.2	8.2	3.7
Spleen	2.6	1.1	0.7
Bone	57.8	56.5	68.7
Heart	7.1	3.5	1.3
Lung	3.7	1.5	0.9